

# Integrating convolutional neural network and constitutive model for rapid prediction of stress-strain curves in fibre reinforced polymers: A generalisable approach

Zerong Ding <sup>a</sup>, Hamid R Attar <sup>a</sup>, Hongyan Wang <sup>a</sup>, Haibao Liu <sup>b</sup>, Nan Li <sup>a,\*</sup>

<sup>a</sup> Dyson School of Design Engineering, Imperial College London, London SW7 2DB, UK

<sup>b</sup> School of Engineering and Materials Science, Queen Mary University of London, London E1 4NS, UK



## ARTICLE INFO

### Keywords:

Representative volume element  
Convolutional neural network  
Fibre reinforced polymer  
Microstructure-property linkage  
Constitutive model  
Unidirectional composites

## ABSTRACT

Despite recent advancements in using machine learning (ML) techniques to establish the microstructure-property linkage for composites' representative volume elements (RVEs), challenges persist in effectively characterising the effect of microstructural randomness on material properties. This complexity arises from the difficulty of expressing randomness as definitive variables and its intertwined relations with other factors, such as material constituents. Such complexities result in limitations in generalising ML models across different material constituents. Conventional solutions to these challenges usually necessitate large datasets, which require considerable computational resources, for an accurate and generalisable ML models to be trained. This paper presents an innovative approach to tackling these challenges by integrating a high-accuracy convolutional neural network (CNN) with a novel microstructure-factored constitutive model (MCM). The MCM, rooted from classic empirical constitutive modelling, effectively segregates the microstructural and constituting material effects, extending the generalisability and thus significantly enhancing the efficacy of the CNN. This new approach enabled a CNN trained on the transverse stress-strain curves of one set of material constituents (CF/PEEK at 270 °C) to be generalised for the rapid prediction of various sets of material constituents at different temperatures, unseen by the CNN during training, with an average mean absolute percentage error around 3 %.

## 1. Introduction

Fibre-reinforced polymers (FRPs) are gaining popularity in transportation industries due to their excellent mechanical properties, such as high strength-to-weight ratio. However, designing FRP components in these sectors often involves multiple iterations of finite element (FE) simulation to evaluate and enhance structural efficiency and manufacturability [1–3]. Modelling and simulating the heterogenous FRPs is usually computationally expensive due to the detailed representations needed to capture the complex microstructures of the fibres, matrix, and the fibre-matrix interface [4,5].

Homogenisation, a process that replaces the heterogeneous composites with a kind of equivalent material model [6], is commonly used to reduce the computational cost. The Rule of Mixture (ROM), among the oldest methods, can quickly estimate the upper and lower bounds of the composites' elastic properties analytically [7]. Due to their simplicity, the ROM can capture only the fibre volume fraction of

composite materials, and struggles with more complex microstructural features such as the random spatial distribution of fibres. In addition, the accuracy of ROM models, particularly in estimating non-linear plastic behaviours, is limited. To overcome these limits, numerical multi-scale modelling has been extensively studied. In a multi-scale modelling scheme, macroscopic structural simulations use homogenised effective material models that are derived from microscopic models [6]. A popular derivation method is FE simulation using representative volume elements (RVEs) [8,9]. The effective properties of an RVE, which is a finite microscopic region with similar characteristics to the macroscopic material sample, are used to approximate the homogenised properties of the entire sample. However, the effective properties of RVEs show considerable variation due to the randomness of microstructural features, particularly when the RVE size is relatively small [10,11]. Although these variations can be adequately characterised through simulating a RVE of a larger size or a large amount of smaller RVEs, their utilisation demands substantial computational resources, especially

\* Corresponding author.

E-mail address: [nan.li@imperial.ac.uk](mailto:nan.li@imperial.ac.uk) (N. Li).

when different material constituents are considered. This computational inefficiency imposes practical limitations, especially in design and optimisation phases, where rapid iterations are of particular importance.

To facilitate a rapid prediction the RVEs' effective properties, researchers have turned to machine learning (ML) models to capture the microstructure features and establish the microstructure-property linkage [12,13]. Ding et al. [14] used a deep neural network (DNN) to find the correlation between the fibre volume fraction, fibre radius of RVEs and the effective elastic modulus and yield strength of the FRP. However, the DNN could not recognise or predict the effect of fibre spatial distribution. Pathan et al. [15] established the correlation between the effective elastic properties and RVE microstructures, including fibre diameter, volume fraction, and spatial distribution. In their study, two-point correlation function (TPCF) and principal component analysis (PCA) were used to reduce the input dimensionality from images to vectors of principle components (PCs). With the inputs being the PCs and targets being the elastic properties, a gradient boosting regressor (GBR) model was trained. The trained GBR model can effectively predict the elastic properties accurately for different fibre volume fractions. However, the prediction accuracy for fibre spatial distribution was not as satisfactory. Li et al. [16] pre-processed the input using similar dimension reduction techniques including TPCF and PCA. In the dataset, they used more complex input data by including the microvoids defect in the matrix when generating the dataset. The training targets were also the elastic properties of the RVEs. They improved the prediction accuracy by using a genetic algorithm optimised back propagation (GABP) network, which optimised the initial network parameters of the network when the training started. Recently, convolutional neural network (CNN) has seen increasing use in capturing the image features in the domain of solid mechanics [17–19], especially in establishing the microstructure-property linkage. Li et al. [20] fused a CNN and a multi-layer perceptron (MLP) model to captures features from both the microstructures and their TPCF outputs for predicting elastic properties of composite materials. Yang et al. [21] trained a CNN with a dataset comprising mosaic-like two-phase microstructures with the same volume fraction to predict the effective stress-strain curve. They performed PCA to reduce the dimensionality of the complex nonlinear stress-strain curves in the targets. The PCs predicted by the trained CNN were then used to reconstruct the stress-strain curve. The model had good prediction accuracy, although some detail features in the non-elastic region were not captured and predicted due to dimensionality reduction. Kim et al. [22] modelled the fibre-matrix interface when generating the dataset, which also led to nonlinear effective stress-strain curves. They trained a CNN with the generated dataset, which showed very high accuracy in the elastic region, although slight deviation can be seen in the plastic region. Xu et al. [23] used a knowledge input transfer learning (KITL) framework by training a CNN in two steps: pre-training and fine-tuning. This framework improved the training efficiency with a reduction of dataset size. Olivier et al. [24] used a Bayesian neural network to quantify the uncertainties of the effective stress-strain curve. Krokos et al. [25] used a Bayesian CNN framework to predict the stress field of RVEs.

Although using ML techniques to establish the microstructure-property linkage has advanced significantly in recent years, there remain two major challenges. The first challenge lies in accurately predicting the effective properties that account for the microstructural randomness. For FRP, variables like fibre diameter and volume fraction have definite values and clear impact on effective properties. However, it is far more challenging to ascertain an accurate relationship between the random fibre spatial distributions, which resemble real FRP materials, and their corresponding effective properties. This is particularly true for the non-elastic behaviours of RVEs. The second challenge concerns the generalisation capability of the ML models. Typically, to learn microstructure-property linkage, an ML model is trained on a dataset generated by simulation RVEs with diverse microstructures, using a

fixed set of material constituents at a specific temperature. However, the model's effectiveness may decline when the properties of these constituents change. For instance, this could occur if the polymer matrix switches from Poly-Ether-Ether-Ketone (PEEK) to Polyamide 6 (PA6), or if the material is used at a different temperature. This limitation necessitates the retraining the model on new datasets, which can impede the models' practicality due to the substantial computational resources required for new simulations.

This paper aims to develop an innovative approach to address the two aforementioned challenges. This approach integrates a convolutional neural network (CNN) with a novel microstructure-factored constitutive model (MCM), to enable the rapid prediction of effective properties of fibre reinforced polymers RVEs with random fibre distributions and to allow generalisation to new constituting materials. In particular, the MCM, rooted from classic empirical constitutive modelling, is a new concept proposed in this study, which can explicitly segregate the intertwined effect of material constituent properties and the effect of fibre spatial distributions. The new approach enabled a CNN trained on the transverse stress-strain curves of one set of material constituents (CF/PEEK at 270 °C) to be generalised for various sets of material constituents at different temperatures, which were unseen by the CNN during training. By incorporating the MCM, the CNN's applicability when serving as a surrogate model in multi-scale simulation schemes can be significantly expanded, which is considered the main contribution of the work.

In this paper, the generation of microstructures, characterising RVE's properties using simulations, as well as post-processing, were discussed in section 2, followed by the implementation, training, and evaluation of a CNN in section 3. Section 4 discussed the development and validation of the MCM. In section 5, a rapid prediction framework was established by integrating the trained CNN with the developed MCM and was validated through testing on random RVEs with various constituting materials.

## 2. Microstructure generation and microstructure-property characterisation

To facilitate the development of the ML model and the microstructure-factored constitutive model (MCM), it is necessary to generate datasets consisting of RVEs with random microstructures and their corresponding effective stress-strain curves. This section details the process of creating such datasets, starting with the development of a novel microstructure generation algorithm. The generated microstructures were then statistically characterised before being modelled as RVEs using FE packages ABAQUS/CAE. Subsequently, the RVEs were simulated under the transverse tensile condition and the resulting data was extracted for the development of the ML model and the MCM.

### 2.1. Microstructure generation algorithm and statistical characteristics analysis

RVE simulations which investigate the effect of microstructure on the effective properties start with generating distinctive microstructures. These microstructures are often generated by microstructure generation algorithms, such as hard core model (HCM) [26], random sequential expansion (RSE) [27]. These algorithms utilised random number generators to generate the coordinates of fibres within a pre-defined space, thus preferred when distinctive microstructures are required. However, the probability of two microstructures randomly generated using these algorithms being nearly identical to each other is extremely low. This means the effect of minor microstructural differences, which can be introduced as observation error such as when capturing real-life FRP microstructures using microscopes, cannot be accounted for. Although the assumption of statistical equivalency [9] suggests that RVEs with similar microstructure should have similar effective mechanical properties, discrepancies were found in this study.

**Table 1**

Pseudocode of the new algorithm for generating similar microstructures.

1. Input: RVE size =  $33 \mu\text{m}$ , fibre diameter ( $d_f$ ) =  $6.6 \mu\text{m}$  [30], number of fibres ( $N$ ) = 16.
2. Generate the coordinates of a ‘base’ microstructure  $X, Y$  using RSE, with  $\min(\text{fibre distances}) = 0.8 \mu\text{m}$
3. FOR  $i = 1 : N$  DO
4.      $\Delta x = \text{random}(\text{perturbation range}(0 \sim 0.49 \mu\text{m}))$
5.      $\Delta y = \text{random}(\text{perturbation range}(0 \sim 0.49 \mu\text{m}))$
6.     Perturbed fibre centre coordinates:  
 $(\tilde{X}[i], \tilde{Y}[i]) = (X[i] + \Delta x, Y[i] + \Delta y)$
7. End FOR
8. If  $\min(\text{fibre distances}) < 0$ :
9.     Repeat step 3–7
10. Else:
11.     Output  $\tilde{X}[i], \tilde{Y}[i]$

A new algorithm was proposed in this study to generate microstructures, combining both distinctive and similar fibre distributions. This algorithm was automated by a Python script to produce a considerable number of diverse microstructures and their variants. The automated generation process is given in Table 1. The input parameters given in step 1 ensured a relatively small RVE size of 10, defined by the ratio between the side length of the RVEs and the fibre radius. Additionally, a total of 16 fibres was generated so that the fibre volume fraction in all generated microstructures was 51 %. It should be noted that these definitive microstructural variables, including fibre diameter and number of fibres, were deliberately kept constant so that the random fibre spatial distribution was the only microstructural variables in the dataset. This setup presented the most challenging scenario for training an accurate CNN. Step 2 used RSE algorithm with geometric periodicity [27,28] to generate a distinctive random ‘base’ microstructure. To avoid fibre overlapping,  $0.8 \mu\text{m}$  was set as the minimum allowable fibre distance in the RSE algorithm, where the term ‘fibre distance’ was defined as the nearest distance between the outer edges of two fibres. Based on the ‘base’ microstructure, a variant could be generated through steps 3–7. In these steps, the coordinates of each fibre in the ‘base’ microstructure were randomly perturbed, and the perturbation range in both  $x$  and  $y$  directions for each was defined as  $0 \sim 0.49 \mu\text{m}$ . The minimum fibre distance in a variant microstructure was calculated using the nearest neighbour distance [29] and examined in step 8. If the minimum fibre distance was found to be smaller than 0, indicating fibre overlapping, the generated variant was rejected. Step 3–7 were then repeated until a

variant microstructure with the minimum fibre distance larger than 0 was successfully generated. Fig. 1a) illustrates the perturbation process, while Fig. 1b–d) shows an example of a ‘base’ microstructure and one of its variants. Using the introduced method, 2000 ‘base’ microstructures, which are distinctive from each other, and 5 similar variants for each ‘base’ microstructure were generated.

To evaluate the preservation of the statistical characteristics of the microstructures after perturbations, the two-point correlation function (TPCF) of the microstructures was calculated, and their outputs were compared. The TPCF is a statistical measure to describe matter distribution [31] and has been recently utilised to measure the fibre distribution in RVEs [15,16]. It is defined as the probability of finding fibres on both ends of a vector, that is randomly thrown into the microstructure. The mathematic form of the TPCF is written as:

$$f(\mathbf{r}) = \frac{1}{S} \sum_{s=1}^S \omega_s \omega_{s+\mathbf{r}} \quad (1)$$

$$\omega = \begin{cases} 1, & \text{material phase at subscripted pixel is fibre} \\ 0, & \text{material phase at subscripted pixel is matrix} \end{cases} \quad (2)$$

where  $\mathbf{r}$  is a vector,  $S$  is the total number of the pixels in the microstructure image space. The vector enumerates the whole pixel space to find the material phase  $\omega$  at the starting pixel  $s$  and the ending pixel  $s + \mathbf{r}$ . The value of  $\omega$  is defined in Equation (2) [15]. The output of the TPCF is an array of the same size of the microstructure image, and it can also be visualised as an image, as demonstrated in Fig. 2a). It is worth noting that when  $\mathbf{r}$  is the zero vector, i.e., a vector with zero length, the materials on both ends of the vector, wherever the starting point  $s$  is, are the same, i.e.,  $\omega_s = \omega_{s+\mathbf{r}}$ . Therefore, the value of  $f(\mathbf{0})$  is the fibre volume fraction of the microstructure. The fibre volume fraction can be observed in the centre (representing the zero vector) of the image representation of the TPCF output, as shown in Fig. 2a).

Fig. 2a) depicts three pairs of ‘base’ and one of their variant microstructures, with a pair of regular fibre distribution and two pairs of arbitrarily chosen random microstructures, along with their TPCF outputs. It is visually evident that each pair is distinctive, and for each pair, the ‘base’ microstructure and its variant microstructure are similar and have nearly identical TPCF outputs. The similarity was further examined quantitatively by computing the structural similarity (SSIM) index. The SSIM index is a perceptual metric that quantifies the difference between images, ranging from -1 to 1, where 1 indicates that two images are

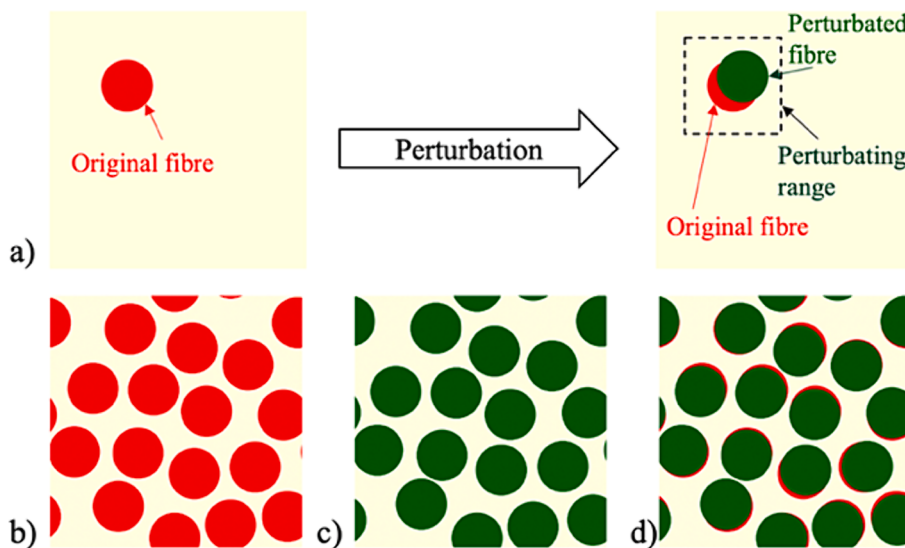


**Fig. 1.** A) the schematic illustration of perturbing a fibre; an example of b) a ‘base’ microstructure and c) a variant microstructure after fibre perturbation, and d) overlay of the base and variant microstructures showing small differences.

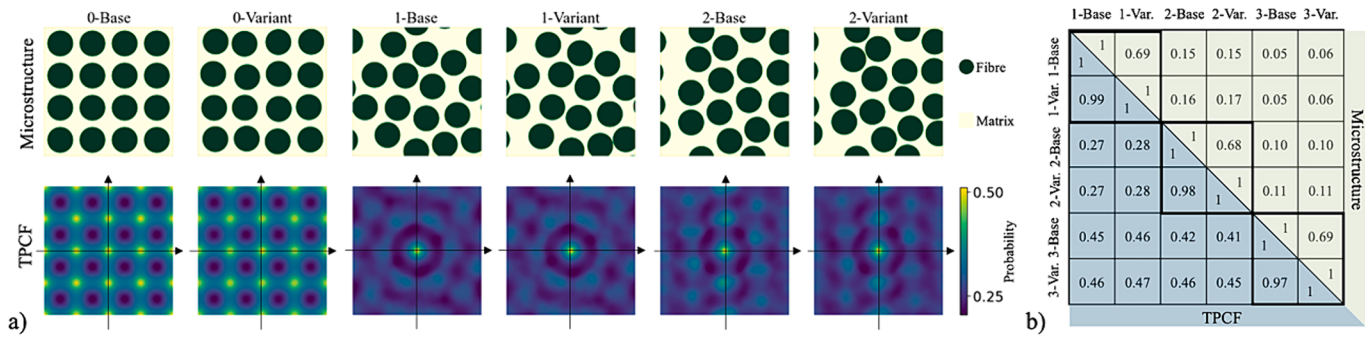


**Fig. 2.** A) three example sets of microstructures (with the ‘base’ and a variant for each set) and their two-point correction function (TPCF) presentations, and b) their structural similarity (SSIM) when comparing to each other.

identical. In this study, the SSIM index was computed using the *ssim* function from the Scikit-image package, and the algorithm is detailed in [32]. Fig. 2b) shows the SSIM indices between the microstructures (upper diagonal) and their TPCF outputs (lower diagonal). The SSIM indices between each ‘base’ and its variant microstructure, as well as their TPCF outputs, are noticeably higher than those between distinctive microstructures. Moreover, the SSIM indices between the TPCF outputs of each ‘base’ and its variant microstructure are nearly 1, demonstrating that the statistical characteristics of the microstructures are well preserved in this perturbation process.

## 2.2. Finite element simulations of the RVEs and post-analysis

The generated microstructures were modelled as RVEs and numerically simulated under transverse tensile conditions using the FE package ABAQUS/CAE. The resulting simulations were post-processed to obtain the effective stress-strain curves. To automate the simulation process, a set of Python scripts were developed, allowing for the simulation of a large batch of 10,000 variant microstructures. Additionally, to ensure consistency in the dataset, only ‘variants’ but not the ‘base’ microstructures were simulated, because their fibre distance criteria were altered from their respective ‘base’ microstructure due to the fibre perturbation.

Fig. 3 presents a typical RVE simulation process. The simulation commenced with the generation of the geometric model of the microstructure. Subsequently, the geometric model was meshed using a unified meshing strategy with an approximate mesh size of  $0.66\text{ }\mu\text{m}$ . The fibre-matrix interfaces were assumed as perfect bonding interfaces modelled using a shared-nodes approach. This simplification was inspired by recent studies handling similar problems [21,23,24]. The plain strain CPE4R elements were used to model both fibre and matrix regions. The final step involved assigning constituting materials to the meshed model to create an RVE.

In this paper, the term “constituting material” refers to the set of material constituents of the RVE at a given working temperature. Each constituting material was treated as an individual material as their thermomechanical responses are different due to different temperatures, even though they represent the same matrix. To simplify the naming

convention for the materials with their constituents, the format of Fibre/Matrix-Temperature, e.g., CF/PEEK-270, is used hereinafter.

The carbon fibre used in this study was reasonably taken as temperature-independent, and its properties are listed in Table 2. Two matrix materials, PEEK and PA6, were employed. Their material properties were obtained from in-house experiments [33]. It was found that the thermomechanical responses of the two matrix materials are highly temperature dependant and are insensitive to the strain rate. Therefore, their behaviours were modelled with the Johnson-Cook plasticity model [34]:

$$\sigma_f = [A + B(\bar{\varepsilon}^{pl})^n](1 - \hat{\theta}^m) \quad (3)$$

where  $\sigma_f$  is flow stress,  $\bar{\varepsilon}^{pl}$  is plastic strain, and  $A, B, n, m$  are material constants.  $\hat{\theta}$  is a normalised dimensionless term corresponding to working temperature defined as:

$$\hat{\theta} = \begin{cases} 0, & \theta < \theta_{ref} \\ (\theta - \theta_{ref}) / (\theta_m - \theta_{ref}), & \theta_{ref} \leq \theta \leq \theta_m \\ 1, & \theta > \theta_m \end{cases} \quad (4)$$

where  $\theta$  is the current temperature,  $\theta_m$  is the melting point and  $\theta_{ref}$  is the reference temperature of the matrix. The elastic moduli and material constants that were determined from the experimental results are listed in Table 3.

To prepare a dataset for the subsequent ML training, which will be detailed in Section 3, simulations were conducted for all 10,000 RVEs using the CF/PEEK-270. In addition, a few RVEs with different constituting materials were simulated to develop the MCM, which will be detailed in section 4.

After the geometric modelling and meshing of the RVEs, periodic boundary conditions (PBCs) were applied using the ABAQUS plugin easyPBC [36]. The PBCs allowed the simulation of an RVE under transverse tensile condition, where an effective transverse strain of 0.05 was applied. The deformation problem under these boundary conditions was solved, followed by the post-processing of the simulation result.

A Python script was developed for post-processing the simulation results and extracting the true effective stress-strain curve of each RVE. The curve was then discretised into a vector of effective stress values at

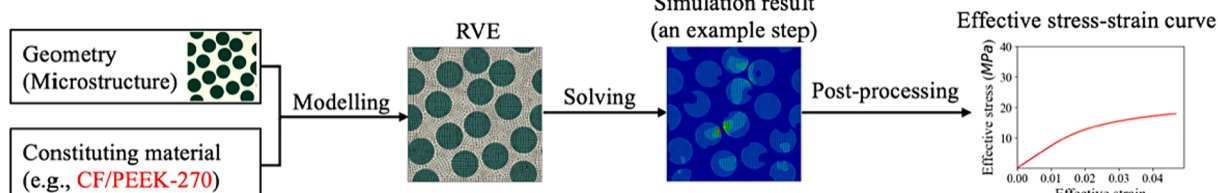


**Fig. 3.** A typical representative volume element (RVE) simulation scheme.

**Table 2**

Material properties of carbon fibre [35].

E11/E22 (GPa)	E33 (GPa)	v12	v13, v23	G13, G23 (GPa)
26	214	0.445	0.28	112

**Table 3**

Material properties and constants of polymer matrices [33].

Temperature-dependent elastic moduli						
PA6	Temp. (°C)	160	180	200	220	
	E (MPa)	180.13	152.77	78.02	27.79	
PEEK						
	Temp. (°C)	210	240	270	300	310
	E (MPa)	242.96	167.24	155.59	115.68	110.65

Johnson-Cook material constants						
A (MPa)	B (MPa)	n	m	$\theta_{ref}$ (°C)	$\theta_m$ (°C)	
PA6	11.489	14.531	0.729	1.079	160	230
PEEK	15.651	29.079	0.298	0.947	180	343

even intervals of true effective strain between 0 and 0.046, obtained by cubic interpolation. The resulting stress vector had a size of  $1 \times 30$  and will be referred to as such hereinafter.

Fig. 4 shows three example groups of variant microstructures, which

is overlayed on the ‘base’ microstructures for distinction, and their corresponding effective stress-strain curves. Compared to the wide spread of the effective stress-strain curves for all 10,000 RVEs, the variants of the same ‘base’ microstructure, including the regular ones, exhibit much more similar stress-strain responses. However, discrepancies can still be distinguished for some groups, especially in the plastic region.

To quantify the discrepancies in the effective stress-strain curves caused by fibre perturbation for each group, the mean percentage error ( $MPE_p$ ) was calculated for each RVE using Equation (5):

$$MPE_p = \frac{1}{30} \sum_{i=1}^{30} \frac{\sigma_i^p - \sigma_i^{ave}}{\sigma_i^{ave}} 100\% \quad (5)$$

where  $i$  denotes the strain point index of the effective stress vector of length 30,  $\sigma_i^p$  is the effective stress value of a variant RVE, and  $\sigma_i^{ave}$  is the averaged effective stress values of 5 variant RVEs in this group. An example is shown in Fig. 5a).

The  $MPE_p$  were calculated for all simulated RVEs and their statistical distribution is presented in Fig. 5b). The bin width used for the histogram is 1 %. The histogram shows that the majority of RVEs have very small  $MPE_p$  values in their effective stress-strain curves. Specifically, the effective stress-strain curves of 99.6 % of the 10,000 RVEs have  $MPE_p$  values within  $\pm 10$  %, and those of 90.3 % within  $\pm 5$  %.

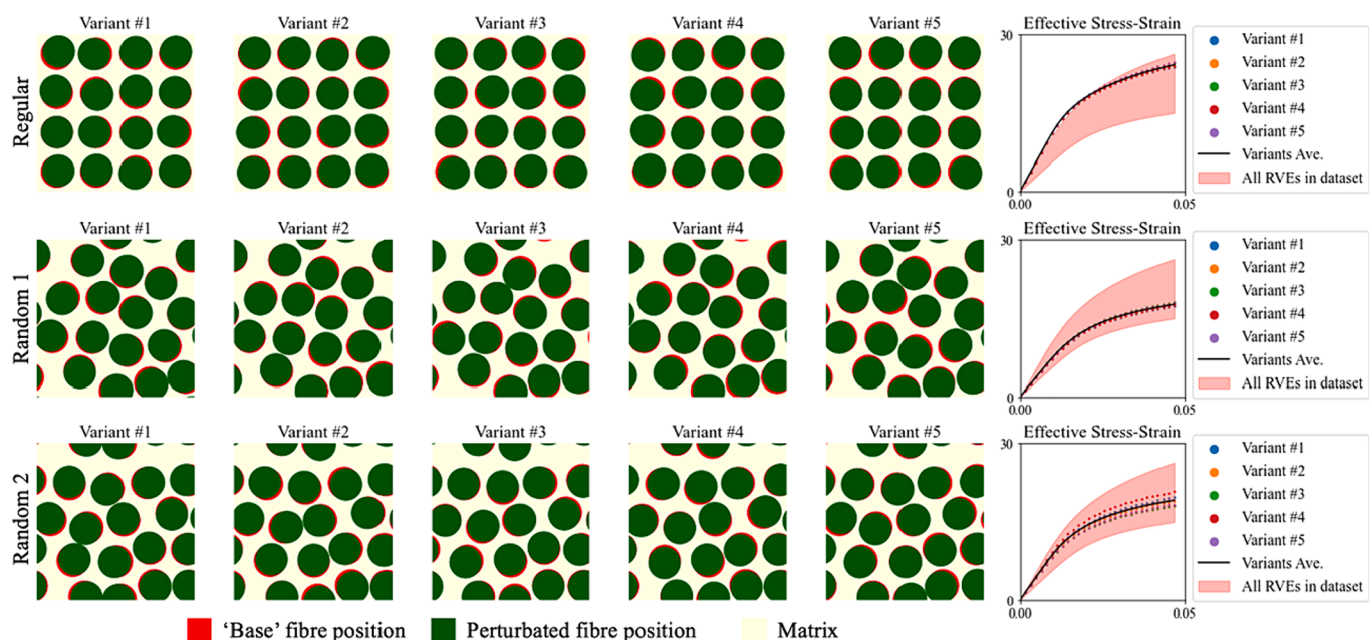


Fig. 4. Effective stress-strain curves of RVEs with three example groups of variant microstructures (pink shadow represents the range of stress-strain curves of all RVEs in the dataset). (For interpretation of the references to colour in this figure legend, the reader is referred to the web version of this article.)

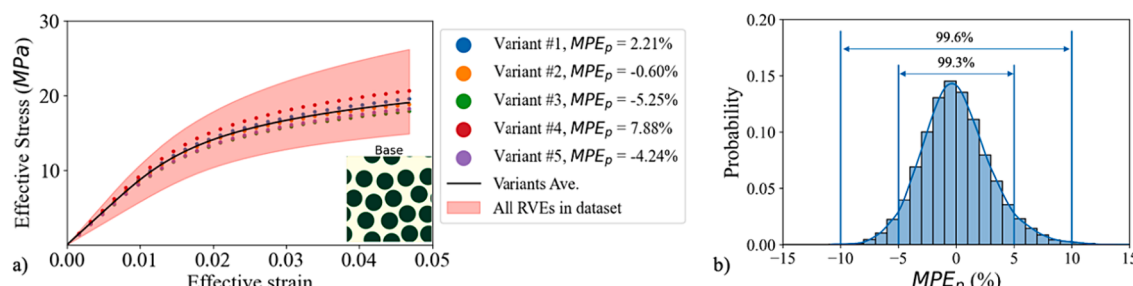


Fig. 5. a) the discrepancies in the effective stress-strain curves of an example group of variant RVEs (pink shadow represents the range of stress-strain curves of all RVEs in the dataset), b) the probability distribution of the mean percentage error ( $MPE_p$ ) caused by perturbation for all RVEs. (For interpretation of the references to colour in this figure legend, the reader is referred to the web version of this article.)

These discrepancies in the effective stress-strain curves, resulting from minor microstructural difference, were relatively small. Nevertheless, there were still a few outliers with discrepancies up to 15.8 %, measured by the absolute  $MPE_p$ . These outliers didn't display noticeably larger microstructural differences compared to other variants sharing the same 'base' but led to relatively larger discrepancies in effective stress-strain curves. It could potentially complicate the training of an accurate ML model. Therefore, the average of the stress-strain curves of each group of variant RVEs were deemed to be a suitable approximation for all variants sharing a same 'base' microstructure in the following study.

### 3. Convolutional neural network: learning the effect of random microstructural distributions for effective property predictions

#### 3.1. Preparation of the dataset

To train the ML model, RVEs with  $2000 \times 5$  microstructures and their corresponding effective stress-strain curves when the constituting material was CF/PEEK-270 were used to create the dataset. The microstructures of the RVEs were discretised into binary arrays with the size of  $128 \times 128$  as inputs to the ML model. This array size was proven to be sufficient in this study to train an accurate convolutional neural network (CNN). In these binary arrays, the numbers '1's denote the fibres and '0's denoted the matrix. The corresponding stress vectors, as described in section 2.2, were of a length of 30. These vectors were used as targets to train the ML model.

The dataset was divided into training and testing sets, using a 90 % training and 10 % testing split. The training set was further divided into 9 folds for the cross validation during training, while the testing set remained unseen during the training process and was reserved to evaluate the final trained model.

In addition, each batch in the training set consisted of 4 groups of variant microstructures and corresponding stress-strain curves, with a batch size of 20. An example batch is shown in Fig. 6. As mentioned in section 2.3, the stress vectors used as targets were the average of 5 variant RVEs', with each group of RVEs being assigned the same stress vector.

#### 3.2. CNN implementation and training

A convolutional neural network (CNN) was developed to recognise the microstructures and predict the corresponding stress vectors. Fig. 7 shows the architecture of the developed CNN.

The CNN consisted of three convolutional layer blocks, each using 16 kernels with a kernel size of 3, a stride of 1 and padding of 1, followed by a LeakyReLU and a BatchNormalization layers. A 2D MaxPooling layer was added to the last convolutional layer block's BatchNormalization layer. A GlobalAveragePooling layer was placed after the convolutional layer blocks, followed by a fully connected layer with 30 nodes to match the length of the target stress vector. The Adam optimiser was used to train the network with a learning rate of 1e-3 and weight decay of 1e-5. During training, the optimiser iteratively minimised the mean squared error (MSE) loss function given in Equation (6).

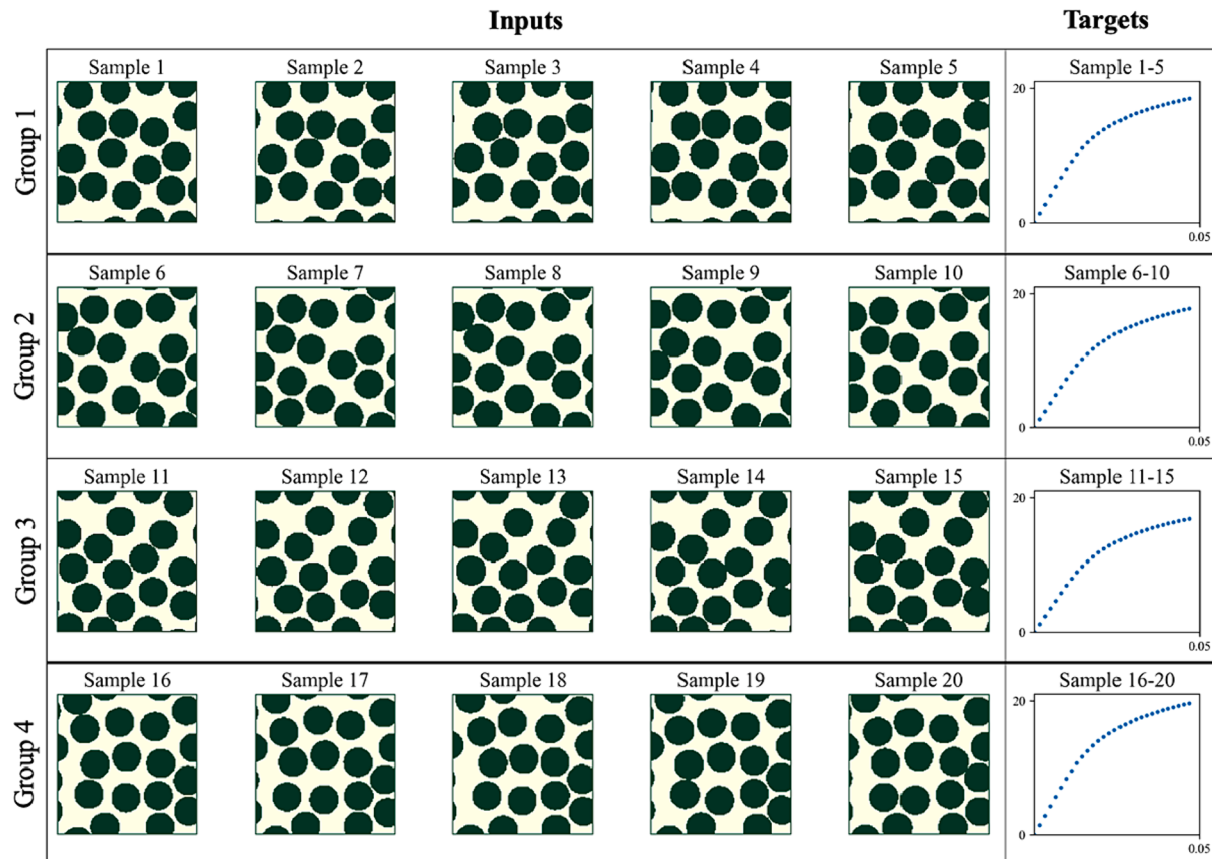
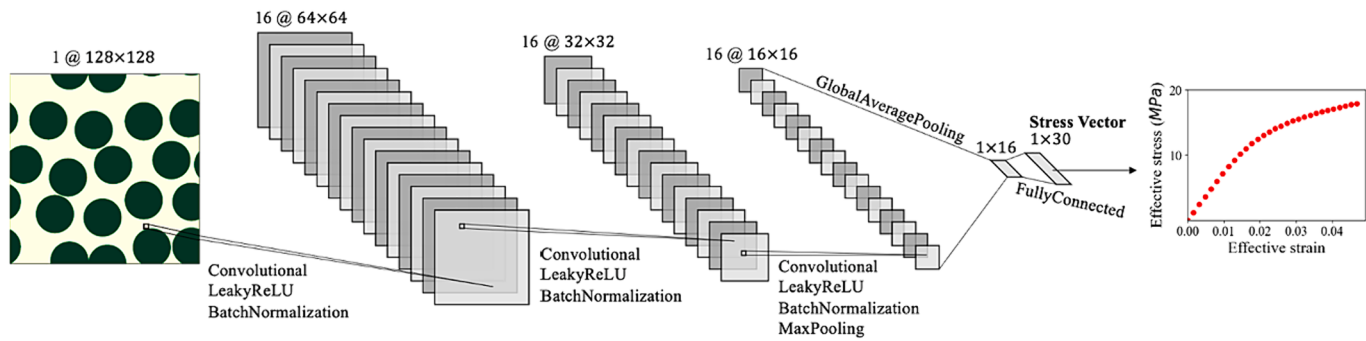


Fig. 6. A batch from the training set, with the inputs being the microstructures of four groups of variants, and the targets being the discretised average effective stress-strain curves of their corresponding groups of variants.



**Fig. 7.** The architecture of the convolutional neural network (CNN) used in this paper.

$$MSE_{\sigma} = \frac{1}{30} \sum_{i=1}^{30} (\sigma_i^{PD} - \sigma_i^{GT})^2 \quad (6)$$

where  $\sigma_i^{PD}$  and  $\sigma_i^{GT}$  are the predicted (PD) and ground truth (GT) stress values at strain point  $i$ , respectively.

The CNN was developed and trained using Pytorch on a NVIDIA Quadro RTX5000 GPU. A 9-fold cross validation technique was implemented during training. The network was trained for 1500 epochs for each fold with the folded validation set being used at every epoch to evaluate the network's performance during the training. For each fold, the model parameters of the network were reset to avoid data leakage. Fig. 8a) shows the training history of Fold 1, with epoch 376 exhibiting the lowest loss in the validation set. The model from this epoch was considered trained for Fold 1. This process was repeated for the other folds. Fig. 8b) compares the model performance of each fold's trained model, and the model from Fold 1 achieved the lowest validation loss across all folds. Therefore, model parameters of Fold 1 at epoch 376 were frozen and assigned to the network as the trained CNN model for the final evaluation using the withheld testing set.

### 3.3. Evaluation of the prediction accuracy of the CNN

Aside from the MSE loss function, additional metrics were used to evaluate the trained model, including the mean percentage error (MPE) and mean absolute percentage error (MAPE) of the stress vectors. These relative error metrics provide a clearer indication of the prediction accuracy. The MPE was calculated using Equation (7).

$$MPE_{\sigma} = \frac{1}{30} \sum_{i=1}^{30} \frac{\sigma_i^{PD} - \sigma_i^{GT}}{\sigma_i^{GT}} \cdot 100\% \quad (7)$$

$MPE_{\sigma}$  indicates both the magnitude and direction of errors, i.e., whether the prediction was overestimated or underestimated. While it is

preferred for evaluating individual predictions,  $MPE_{\sigma}$  may not be accurate when averaged to determine the overall model performance. Therefore, MAPE, defined in Equation (8), was also used as an evaluation metric.

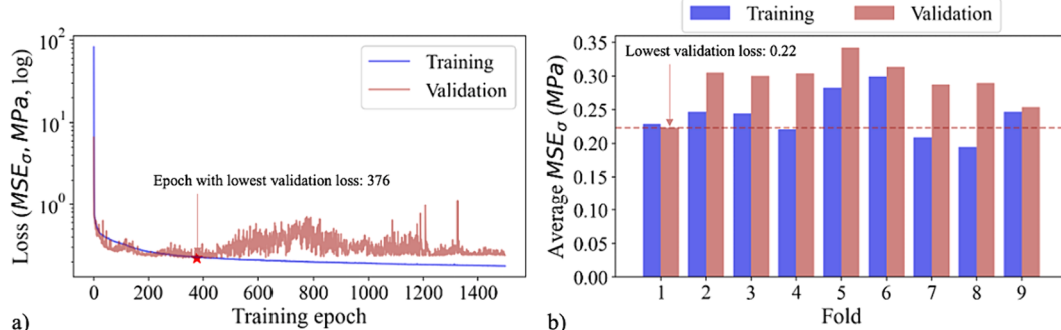
$$MAPE_{\sigma} = \frac{1}{30} \sum_{i=1}^{30} \frac{|\sigma_i^{PD} - \sigma_i^{GT}|}{\sigma_i^{GT}} \cdot 100\% \quad (8)$$

In both Equations (7) and (8),  $\sigma_i^{PD}$  and  $\sigma_i^{GT}$  are the predicted (PD) and ground truth (GT) stress values at strain point  $i$ , respectively.

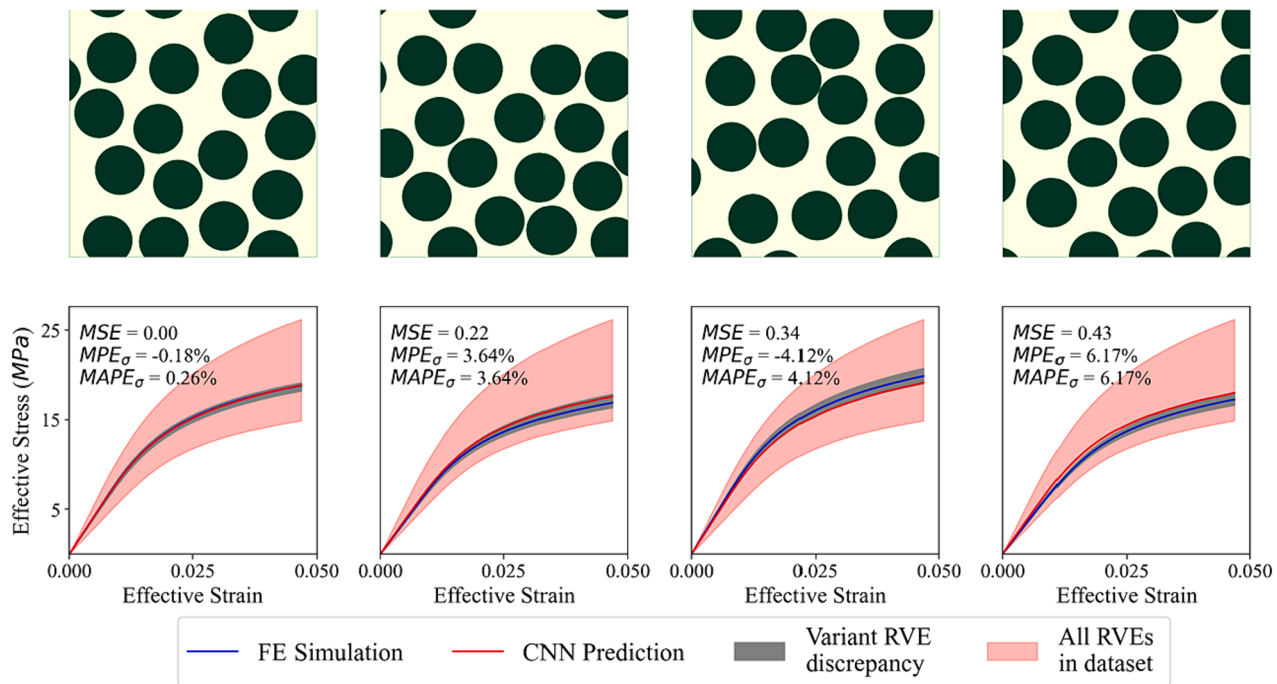
Four examples of the network prediction, arbitrarily selected from the testing set, are shown in Fig. 9. These examples illustrate the high accuracy of the model, as all predictions fall within the range of discrepancies caused by the fibre perturbation.

Fig. 10 shows the overall performance evaluation of the trained network based on the  $MSE_{\sigma}$ ,  $MPE_{\sigma}$  and  $MAPE_{\sigma}$  metrics computed on all data points from both the training and testing sets. The similarities of the statistics between the testing and training sets suggest that the network was trained without overfitting. The prediction accuracy on the testing set was also quantitatively analysed. As shown in Fig. 10a), 95.8 % of the predictions have  $MSE_{\sigma}$  less than 1 MPa. Fig. 10b) shows the  $MPE_{\sigma}$  distribution is approximately normally distributed around 0. For the testing set, 99.4 % of the predictions fall within the error range of  $\pm 10\%$ , and 80.7 % within the error range of  $\pm 5\%$ . These statistics suggest that the network prediction error was on par with the discrepancy caused by the minor microstructural differences. Fig. 10c) shows the  $MAPE_{\sigma}$  distribution. Additionally, the average  $MAPE_{\sigma}$  of the prediction was 3.04 %, and the maximum  $MAPE_{\sigma}$  was 12.83 %.

The findings demonstrate that the developed CNN is highly effective in accurately predicting the effective stress-strain curves by recognising microstructure images. This indicates the potential of using machine learning approaches to predict complex mechanical behaviours of RVEs with random fibre spatial distributions.



**Fig. 8.** A) training history of fold 1, b) the performance of the trained model of each fold using a 9-fold cross validation technique.



**Fig. 9.** Examples of the trained network predictions from the testing set (pink shadow represents the range of stress-strain curves of all RVEs in the dataset, and grey shadow represents the range of stress-strain curves of variant RVEs with similar microstructures). (For interpretation of the references to colour in this figure legend, the reader is referred to the web version of this article.)

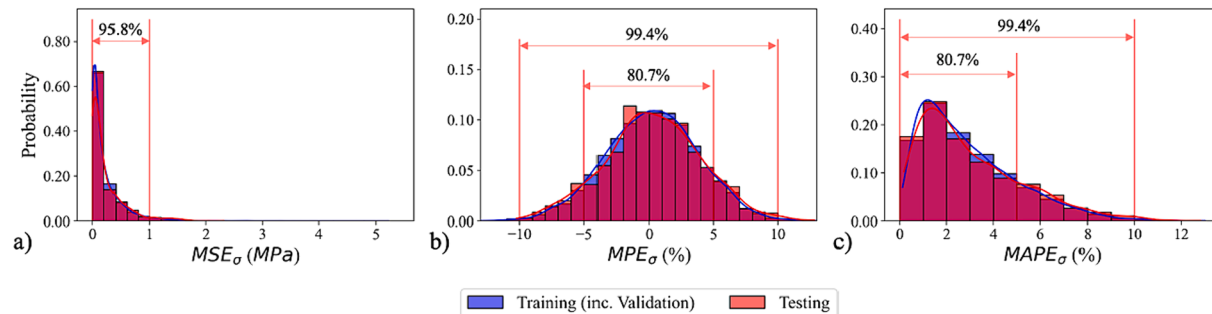


**Fig. 10.** Performance of the trained network evaluated by a)  $MSE_{\sigma}$ , b)  $MPE_{\sigma}$  and c)  $MAPE_{\sigma}$ .

#### 4. Microstructure-factored constitutive model: segregating microstructural and material constituent effects

The work presented in section 3 demonstrates the rapid and accurate prediction of effective stress-strain curves for RVEs with random microstructures using the trained CNN model. However, the model's validity is limited to the CF/PEEK-270 constituting material. Retraining the model for a different constituting material or creating a more generalisable CNN on a dataset of various constituting materials would be costly in terms of data generation.

To overcome this limitation, a Microstructure-factored Constitutive Model (MCM) was developed to segregate the intertwined effects of microstructure and constituting material on the effective properties of a random RVE.

The development and the validation of the MCM were based on analysing the effective stress-strain curves of the RVEs with 50 distinctive microstructures, arbitrarily chosen from the testing set used in section 3, plus the regular microstructure. For each microstructure, RVEs were modelled using 9 different matrix material properties: PEEK at 210, 240, 270, 300, and 310 °C, and PA6 at 160, 180, 200, and 220 °C. In the context of this paper, “constituting material” refers to the set of

material constituents of an RVE at a specific working temperature. This means that 9 constituting materials, such as CF/PEEK-210, CF/PEEK-270 and CF/PA6-180, were adopted for the analysis of each microstructure and treated independently.

##### 4.1. Elastic-plastic behaviours and effective material constants of the RVEs

The development of the MCM started with extracting characteristic material constants, which can also be used for higher-scale simulations, from the effective stress-strain curves of the RVEs based on elastic-plastic material model. For the elastic region, the effective elastic modulus was used. The yield strength was determined by the commonly used 0.2 % offset yield strength (OYS). For the plastic region, as each constituting material was treated independently, the Johnson-Cook plasticity model provided in Equation (3) can be simplified by removing the temperature-dependant term, given as:

$$\sigma_f = A + B(\dot{\epsilon}^{pl})^n \quad (9)$$

The material constant  $A$  presents the yield strength. The strain hardening exponent  $n$  was set to 0.5 for simplicity. The fitting of  $B$  was

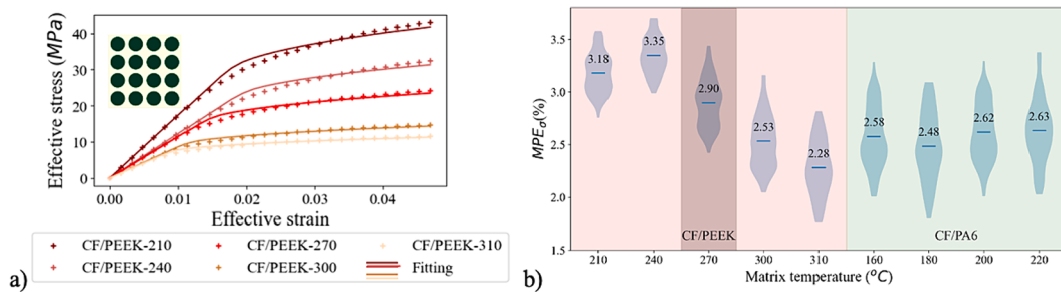


**Fig. 11.** A) fitting material constants for the regular RVEs using varying constituting materials (markers '+' are the simulation results and solid curves are constructed with fitted material constants); b) violin plots depicting the  $MPE_{\sigma}$  of the material constant fitting.

achieved by finding the optimal  $B$  value that minimised the mean squared error (MSE) between the effective stress-strain curve from the simulation and the curve constructed with the elastic–plastic material model. The *least\_squares* function from the Scipy package was employed for the fitting process. Using the method described above, the effective material constants for all  $51 \times 9$  RVEs, representing 51 microstructures and 9 constituting materials, were determined.

The fitting quality is generally satisfactory. Fig. 11a) shows an example of the regular RVEs with varying CF/PEEK constituting materials, with the constructed stress-strain curves showing slight overestimation compared to the simulation results. Fig. 11b) shows the statistics of the fitting errors in RVEs for all 50 random microstructures and 9 constituting materials, measured by calculating the  $MPE_{\sigma}$  between the constructed stress-strain curves and the simulation results. Overall, a fitting error of around  $2 \sim 3.5\%$  was introduced when modelling the stress-strain curves with the traditional material constitutive model. These errors were smaller than either of those caused by fibre perturbation or CNN prediction and will nevertheless be introduced when used in higher-scale simulation with material constitutive models. Therefore, they were deemed insignificant, and the effective materials constants, which were fitted from the simulation results, along with the stress-strain curves constructed using these effective material constants, were henceforth taken as the ground truth (GT).

#### 4.2. The development of the MCM

The effective material constants of random RVEs were analysed, by using those of the regular RVEs as the benchmark. RVEs with two arbitrarily chosen microstructures (denoted as  $\alpha$  and  $\beta$ ) were analysed first with the results illustrated in Fig. 12.

Despite the non-linear behaviours of the constituting materials and intricate deformation patterns in RVEs attributed to random fibre distributions, a noteworthy observation was made. It was observed that the

effective material constants of a given random RVE, including  $E$ ,  $A$  and  $B$ , have approximately positively proportional relationships with the respective effective material constants of the regular RVEs. Proportional trendlines were fitted as shown in Fig. 12. These trendlines are distinctive characteristics of the microstructures, which are independent from the constituting materials. This significant finding helps to segregate the effects of the microstructure and the constituting material, which are previously complex and intertwined factors governing the effective behaviours of the RVEs.

It is worth noting that in Fig. 12c), the markers slightly deviate from the trendline, possibly due to fitting errors when obtaining the plastic material constants. The analysis of the impact of this error is detailed in section 4.3.

These positively proportional relationships can be described mathematically as:

$$E_{mat}^{\phi} = r_E^{\phi} E_{mat}^{reg} \quad (10)$$

$$A_{mat}^{\phi} = r_A^{\phi} A_{mat}^{reg} \quad (11)$$

$$B_{mat}^{\phi} = r_B^{\phi} B_{mat}^{reg} \quad (12)$$

where  $E$  is the elastic modulus,  $A$  and  $B$  are material constants for the simplified Johnson-Cook model. The superscripts are identifiers for the microstructures, where  $reg$  presents the regular microstructure and  $\phi$  presents a random microstructure, such as  $\alpha$  and  $\beta$ , as shown in Fig. 12. The subscript  $mat$  is the identifier of constituting materials, such as CF/PEEK-270.  $r_E^{\phi}$ ,  $r_A^{\phi}$  and  $r_B^{\phi}$  are the slopes of the trendlines, corresponding to  $E$ ,  $A$  and  $B$  respectively, for a RVE with a random microstructure  $\phi$ . They are defined as microstructure effect factors hereinafter.

These relationships, in conjunction with traditional elasticity and the simplified Johnson-Cook model, constitute the microstructure-factored constitutive model (MCM). As a novel concept, the MCM employs

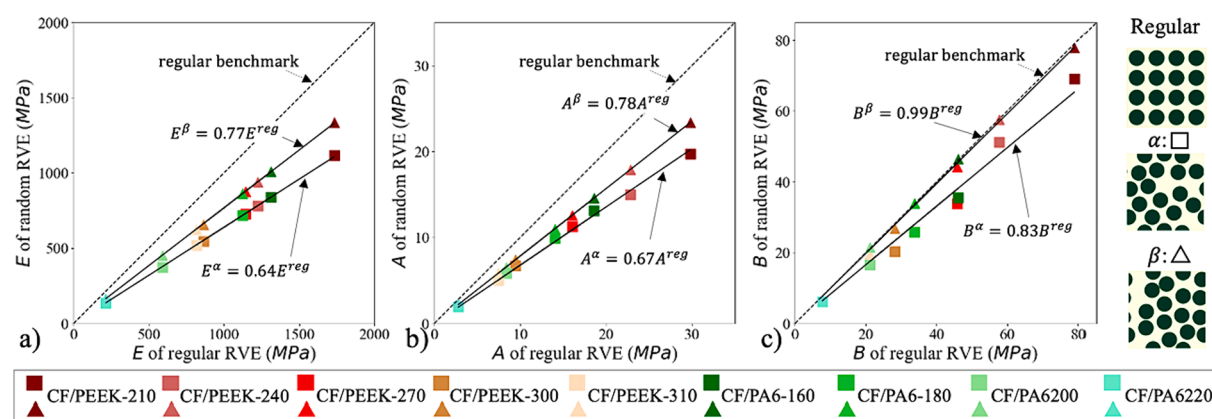


**Fig. 12.** The relationships between random RVEs and the regular RVE with respect to a)  $E$ , b)  $A$ , and c)  $B$ , represented across a range of different constituting materials.

**Table 4**

The workflow of applying the microstructure-factored constitutive model (MCM).

1. Obtain the GT effective material constants of RVEs of the same constituting material, with a) the regular microstructure and b) a random microstructure
2. Determine the microstructure effect factors of the random microstructure, using the two sets of material constants obtained in Step 1 based on Equations (10–12)
3. Obtain the GT effective material constants of RVE of a target constituting material with the regular microstructure
4. Calculate the PD the effective material constants of RVE of the target constituting material with a random microstructure based on Equations (10–12) again
5. Construct the PD stress-strain curve using the PD effective material constants

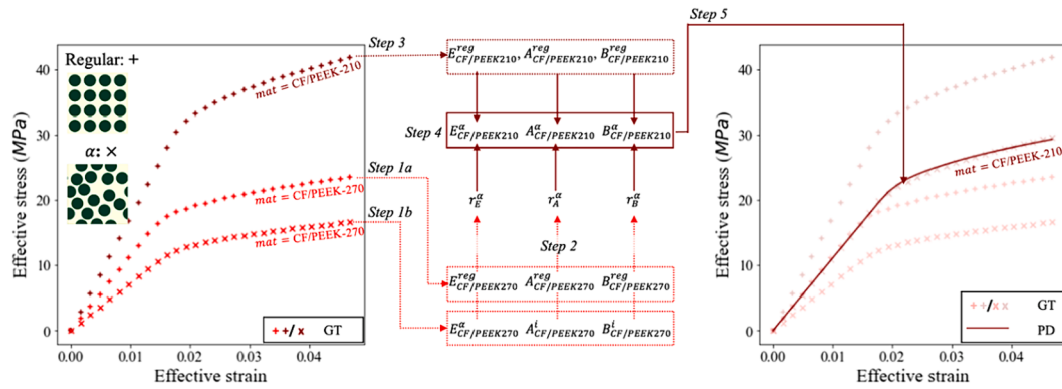


**Fig. 13.** An example of applying the microstructure-factored constitutive model (MCM). GT denotes ‘ground truth’ and PD denotes ‘predicted’.

microstructure effect factors to encapsulate the influence of microstructure, while the effective material constants of the regular RVE are utilised to represent the impact of the constituting material.

**Table 4** outlines the workflow of applying the MCM to predict the effective stress-strain curves of RVEs whenever there is a change in microstructure or constituting material. **Fig. 13** demonstrates an example. As illustrated by the red dotted arrows (Step 1), the process starts with obtaining the ground truth (GT) effective material constants for CF/PEEK-270 RVEs with both microstructures, i.e., *reg* and  $\alpha$ . With these constants, the microstructure effect factors for microstructure  $\alpha$  can be determined based on Equations (10–12) (Step 2). Following the dark red dotted arrow (Step 3), the GT effective material constants of the regular CF/PEEK-210 RVE were obtained. With the microstructure effect factors for microstructure  $\alpha$  and the effective material constants for the regular CF/PEEK-210 RVE known, the effective material constants for CF/PEEK-210 RVE with microstructure  $\alpha$  can be predicted by calling Equations (10–12) again (Step 4). Finally, by plugging the predicted (PD) effective material constants into the elasticity model and simplified Johnson-Cook model, the stress-strain curve can be constructed, as depicted by the solid dark red curve (Step 5). This PD curve shows a good agreement with the GT, as can be seen from the figure.

The illustrated example effectively showcases the efficacy of the proposed MCM in explicitly segregating the intertwined effect of microstructure and the constituting material on the effective properties of random RVE. Consequently, this allows the MCM to predict the effective material constants for any random RVE, given a known microstructure and constituting material. Furthermore, the prediction can be expedited by utilising CNN predictions, instead of FE simulations,

to determine the microstructure effect factors, a process which will be detailed in [section 5](#).

#### 4.3. Evaluation of the prediction accuracy using the MCM

To evaluate the MCM’s applicability to a wider range of microstructures and constituting materials, it was tested on the collection of 50 random microstructures with each of the 9 constituting materials. For each random RVE in this collection, the workflow in **Table 4** was repeated to predict their effective material constants. These PD effective material constants were then compared with the GT values, across all  $50 \times 9$  RVEs, as shown in **Fig. 14**.

To quantitatively measure the average errors in the predicted effective material constants for each constituting material, the mean absolute percentage error,  $MAPE_\psi$ , was defined as given in Equation (13).

$$MAPE_\psi = \frac{1}{n} \sum_{\phi=1}^n \left| \frac{\psi_\phi^{PD} - \psi_\phi^{GT}}{\psi_\phi^{GT}} \right| \cdot 100\% \quad (13)$$

where  $\psi$  can be  $E$ ,  $A$  or  $B$ .  $\phi$  is the microstructure identifier.  $n$  presents the total number of random microstructures and  $n = 50$  here. The values of  $MAPE_\psi$  are listed in **Table 5**. Prediction errors were expected to be 0 for CF/PEEK-270 RVEs, because the microstructure effect factors were determined based on simulations of CF/PEEK-270 regular and random RVEs.

Both **Fig. 14a**) and **Table 5** demonstrate the high accuracy of the developed MCM in predicting the elastic modulus,  $E$ , with all errors less

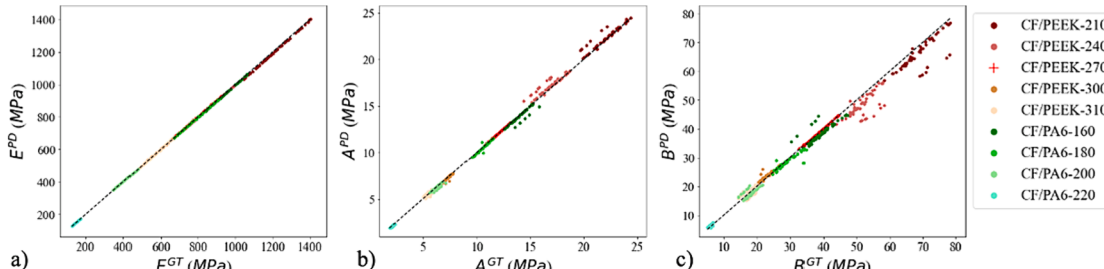


**Fig. 14.** The prediction accuracy of a)  $E$ , b)  $A$  and c)  $B$ , by comparing PD results using the MCM against GT values.

**Table 5**

$MAPE_{\sigma}$ (%) of prediction with microstructure effect factors determined with CF/PEEK at 270 °C.

CF/PEEK	Temp. (°C)	210	240	270	300	310
	E	0.72	0.12	0	0.48	0.35
	A	1.34	2.48	0	1.18	3.06
	B	4.15	7.03	0	3.54	7.91
CF/PA6	Temp. (°C)	160	180	200	220	
	E	0.26	0.02	0.55	0.95	
	A	0.78	0.70	1.34	3.78	
	B	3.95	2.29	5.94	10.50	

than 1 %. The prediction accuracy for the yield strength, A, is fair with all errors less than 4 %. However, the accuracy for B is relatively less satisfying, with the highest error being around 10 %. This discrepancy may be attributed to the fitting error for plastic properties. To further validate the effectiveness of the MCM, the stress-strain curves constructed using the PD and GT effective material constants were compared.  $MAPE_{\sigma}$ , introduced in Equation (8), was used to measure the prediction error.

Fig. 15 shows an example which had the largest prediction error on B when the constituting material was CF/PEEK-210. Despite the relatively large prediction error on B, the stress-strain curves constructed using PD and GT effective material constants were very close, resulting in a small  $MAPE_{\sigma}$ .

Fig. 16 shows the statistics of the prediction errors the statistics of the MCM prediction errors, which are less than 1 %, as measured by  $MPE_{\sigma}$ . The average values of the  $MAPE_{\sigma}$  for all predictions are also below 1 %. These results further validate the effectiveness of the developed MCM.

It is worth noting that while the development and validation of the

MCM were based on changes to matrices and working temperatures, the applicability of the MCM can also be extended to changing fibres, such as glass fibres. This is because the fibres can be treated as rigid bodies due to their high stiffness, which is typically orders of magnitude higher compared to the matrix.

The successfully developed MCM can now be integrated with the trained CNN to construct a rapid prediction framework, in which the CNN can replace the simulations for obtaining the microstructure effect factors in real time. The framework and its streamlined implementation are detailed in the next section.

## 5. A rapid effective property prediction framework integrating the CNN and MCM

Fig. 17 shows the rapid effective property prediction framework integrating the trained CNN and the developed MCM. This framework bypasses the need for expensive simulations for diverse microstructures and enables the prediction of the effective properties of random RVEs with various constituting materials.

Fig. 18 illustrates an example of implementing the proposed framework, using the same microstructure as in Fig. 13. The estimation process is the same, except for one crucial difference: in Step 1b, instead of using simulation results, the stress-strain curve predicted by the CNN is used to obtain the effective material constants for CF/PEEK-270 RVE  $\alpha$  and the subsequent determination of the microstructure effect factors. The PD effective material constants are then used to construct the effective stress-strain curve.

Fig. 19 shows the stress-strain curves of RVEs of all 9 constituting materials, with microstructure  $\alpha$  (first row) and  $\beta$  (second row),

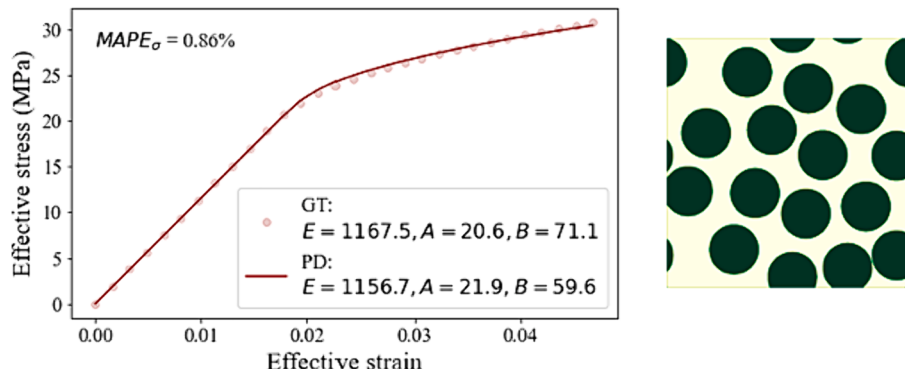


Fig. 15. An example of MCM prediction for a CF/PEEK-210 RVE with a random microstructure.

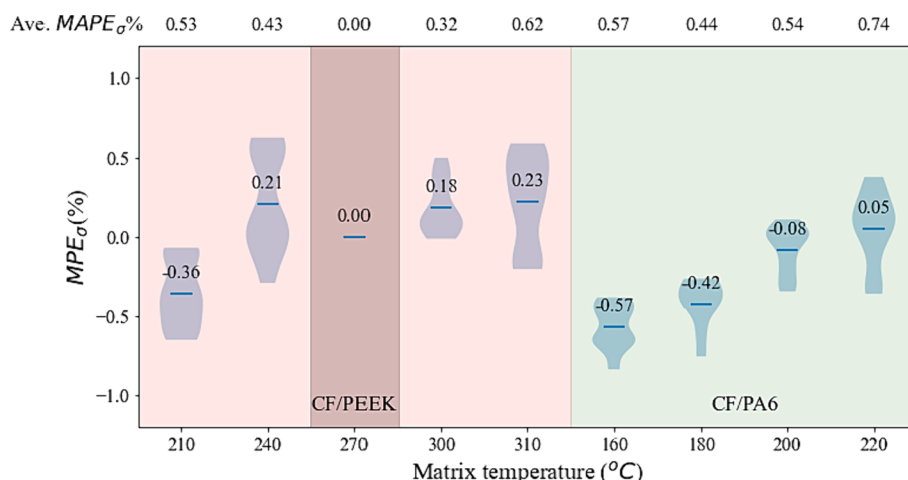


Fig. 16. Violin plots of the  $MPE_{\sigma}$  and the average values of the  $MAPE_{\sigma}$  of the stress-strain responses predicted using the MCM.

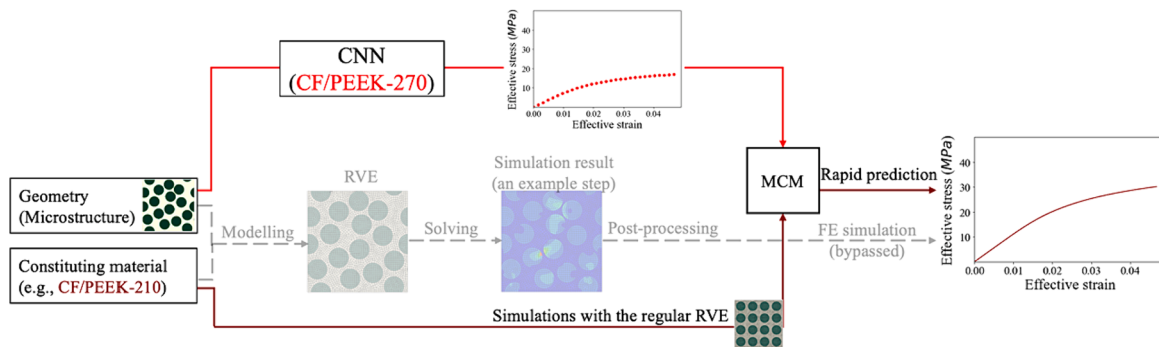


Fig. 17. Rapid prediction framework for predicting the effective properties of random RVEs with diverse microstructures and various constituting materials.

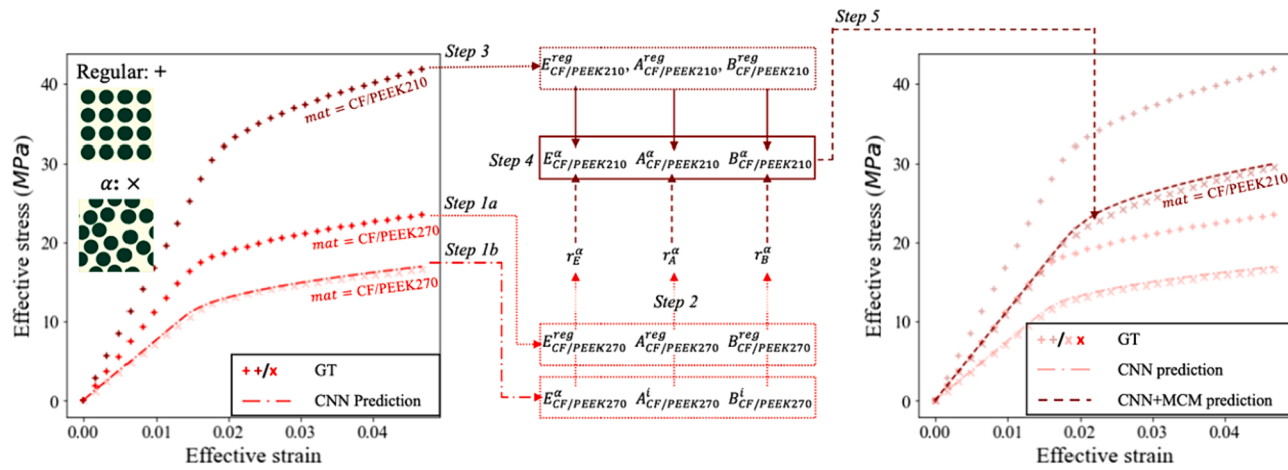


Fig. 18. An example of implementing the rapid prediction framework integrating the CNN and MCM, GT denotes 'ground truth'.

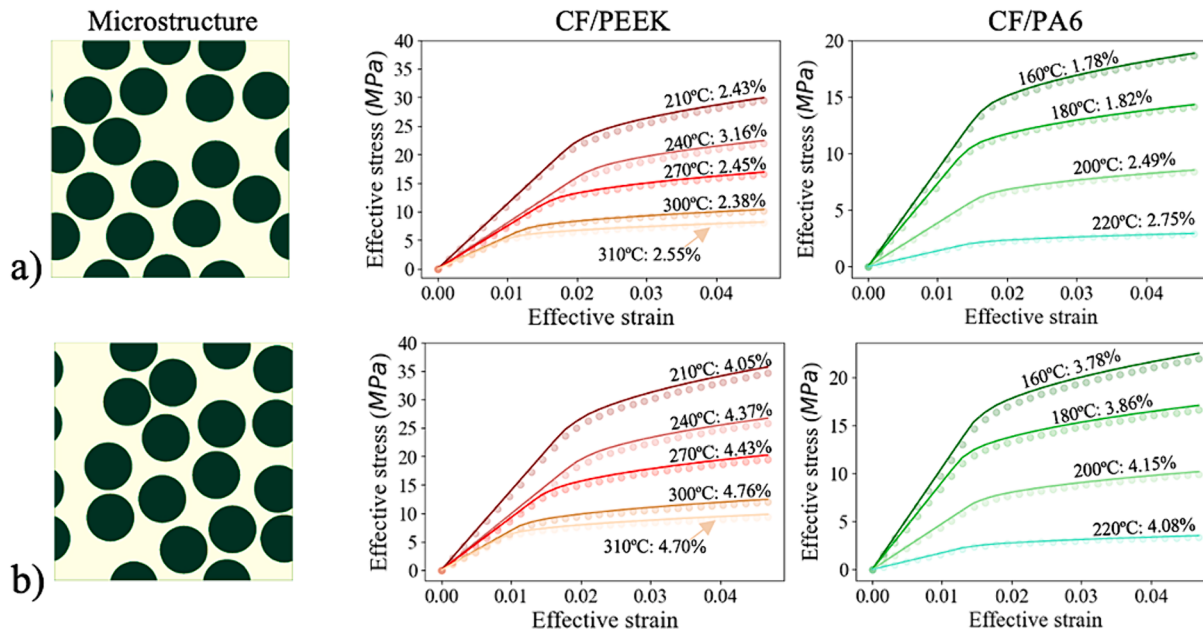
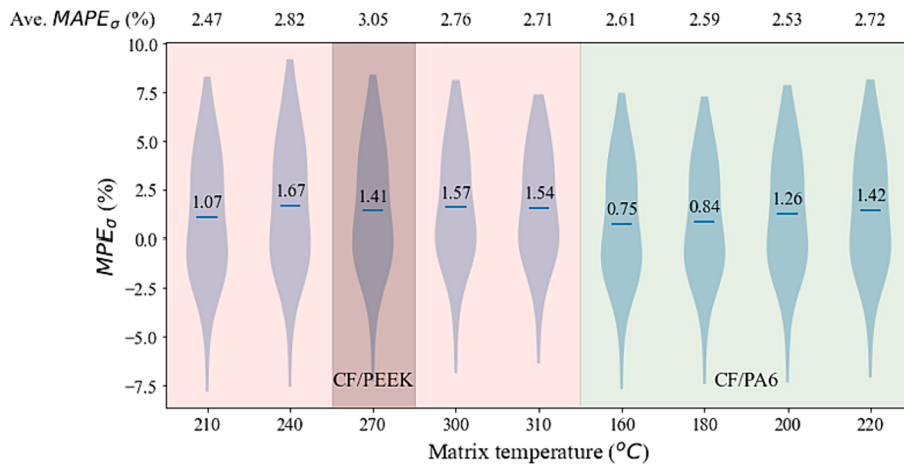


Fig. 19. Rapid predictions made by integrating the CNN and MCM for microstructure a)  $\alpha$  and b)  $\beta$  with corresponding  $MPE_{\sigma}$  provided (dots present GT, curves present PD, and different colours represent different constituting materials grouped as CF/PEEKs and CF/PA6s).

predicted using the rapid prediction framework. The  $MPE_{\sigma}$  for each RVE was calculated between the stress-strain curves constructed using the GT and the PD effective material constants and is given in the figure.

Fig. 20 shows the statistic distribution of  $MPE_{\sigma}$  and the average values of the  $MAPE_{\sigma}$  of the stress-strain curves, as predicted by the rapid

prediction framework integrating the CNN and MCM, across all 50 random microstructures for each constituting material. The results reveal that the maximum absolute value of  $MPE_{\sigma}$  is less than 10 %, and the average values of  $MAPE_{\sigma}$  for all 9 constituting materials are around 3 %.



**Fig. 20.** Violin plots of the  $MPE_{\sigma}$  and the average values of the  $MAPE_{\sigma}$  of the stress-strain response predicted by the rapid prediction framework integrating the CNN and MCM.

While the CNN prediction may introduce errors, resulting in slightly higher error levels shown in Fig. 20 than that in Fig. 16, the overall errors remain small. Furthermore, the errors for all studied constituting materials were at the similar level as the CNN prediction with one constituting material, CF/PEEK-270, which it was trained on. This proves that the introduction of MCM extends the CNN's generalisation capability.

It is worth noting that these 50 microstructures were arbitrarily taken from the testing set used in the CNN training, which represent unseen microstructures, and were employed here to evaluate the performance of the proposed rapid prediction framework. The applicability of this framework is, therefore, not limited to these 50 microstructures but extends to any unseen microstructures. This means, the effective stress-strain curve of a CF/PEEK RVE with any random microstructure distribution can now be predicted in real time without needing to run a FE simulation. Moreover, for a new constituting material, instead of rerunning 10,000 FE simulations to generate a new database for training a new CNN model, only a single simulation on the regular RVE with the new constituting material is required. Once done, this framework integrating the already trained CNN with the novel MCM can be generalised to predict the effective stress-strain responses of RVEs with any unseen microstructures for this new constituting material in real time. Thanks to this new generalisable approach, the computational cost of dataset generation is significantly reduced while maintaining the accuracy. The developed framework significantly expanded the applicability of a CNN when serving as a surrogate model in multi-scale simulation schemes as seen in process simulation and accommodating considerations for diverse materials or working temperatures for process optimisation. In such applications, once the microstructure effect factors are determined based on local microstructures, the effective material constants can be calculated and assigned as local material properties in upper-scale simulations using the Johnson-Cook model, which is readily available in most FE packages.

## 6. Conclusions

This study presents a framework that integrates a high-accuracy convolutional neural network (CNN) with a novel microstructure-factored constitutive model (MCM), enabling the rapid prediction of effective properties of fibre reinforced polymer RVEs with random fibre distributions and, for the first time, generalisation to new material constituents at different temperatures. The main conclusions are drawn as below:

- 1) A new algorithm was introduced to generate both distinctive microstructures and their similar variants through fibre perturbation. Its efficiency was demonstrated by assessing the generated microstructures and their statistical characteristics (two-point correlation function) using the structural similarity (SSIM) index. These enabled the effective creation of microstructure-property data through RVE simulations.
- 2) A CNN was developed and trained using a dataset, which consists of images of variant microstructures and their corresponding stress vectors representing effective stress-strain curves. The CNN, trained using a 9-fold cross validation technique, was found to effectively predict the stress-strain responses of any given microstructures, with a maximum mean absolute percentage error ( $MAPE_{\sigma}$ ) of 12.83 % and average ( $MAPE_{\sigma}$ ) of around 3 % on the testing set. Moreover, 99.4 % of the predictions have their mean percentage error ( $MPE_{\sigma}$ ) within the range of  $\pm 10$  %.
- 3) An MCM was developed to explicitly segregate the intertwined effects of constituting material and microstructure on the effective material properties of RVEs. The model innovatively introduces a new term, microstructure effect factors, to characterise the impact of microstructure. The set of factors of a given microstructure can be determined by comparing the effective material constants of a RVE with the given random microstructure with those of a regular RVE, based on any constituting material. For a random RVE with a specific constituting material, the impact of the constituting material was determined by the effective material constants of its regular RVE. With the microstructure effect factors and the effective material constants of the regular RVE determined, the effective properties of a random RVE can be predicted using the MCM. The MCM prediction errors on the effective stress-strain curves measured by both absolute  $MPE_{\sigma}$  and average  $MAPE_{\sigma}$  were below 1 %.
- 4) A rapid effective property prediction framework was constructed utilising the CNN to capture the effect of random microstructure features and the MCM to integrate the effects of microstructures and constituting materials. This framework extended the generalisation capability of the trained CNN, enabling real time prediction of the effective material properties of RVEs with diverse constituting materials. With this framework, only one simulation is needed with the regular RVE when changing the constituting materials. The maximum absolute  $MPE_{\sigma}$  and average  $MAPE_{\sigma}$  of the rapid framework prediction for all tested RVEs were below 10 % and around 3 %, respectively.

The innovative approach of integrating classic constitutive models with machine learning (ML) models showcases potential and points towards a promising direction for enhancing the generalisability and thus applicability of ML models. Future work can be focused on: extending the developed approach to more sophisticated homogenisation modeling, considering factors such as fibre-matrix interface and micro-defects; broadening the application of the developed approach to a more comprehensive context of material characterisation, encompassing history-dependent material behaviours and different deformation modes.

## CRediT authorship contribution statement

**Zerong Ding:** Writing – original draft, Visualization, Methodology, Formal analysis, Data curation, Conceptualization. **Hamid R Attar:** Writing – review & editing, Methodology, Formal analysis. **Hongyan Wang:** Writing – review & editing, Methodology, Formal analysis. **Haibao Liu:** Writing – review & editing, Supervision, Methodology, Formal analysis. **Nan Li:** Writing – review & editing, Supervision, Project administration, Methodology, Funding acquisition, Formal analysis, Conceptualization.

## Declaration of competing interest

The authors declare that they have no known competing financial interests or personal relationships that could have appeared to influence the work reported in this paper.

## Data availability

Data will be made available on request.

## Acknowledgements

Hamid R. Attar thanks UK EPSRC for the CASE conversion DTP training grant (EP/R513052/1). Hongyan Wang acknowledges the financial support from the Chinese Scholarship Council (CSC) and Imperial College London. For the purpose of open access, the author has applied a Creative Commons Attribution (CC BY) license to any Author Accepted Manuscript version arising.

## References

- [1] P. Boisse, B. Zouari, A. Gasser, A mesoscopic approach for the simulation of woven fibre composite forming, *Compos. Sci. Technol.* 65 (3–4) (2005) 429–436, <https://doi.org/10.1016/j.compscitech.2004.09.024>.
- [2] L. Kärger, S. Galkin, C. Zimmerling, D. Dör, J. Linden, A. Oeckerath, K. Wolf, Forming optimisation embedded in a CAE chain to assess and enhance the structural performance of composite components, *Compos. Struct.* 192 (2018) 143–152, <https://doi.org/10.1016/j.compstruct.2018.02.041>.
- [3] R. Nakka, D. Harursampath, M. Pathan, S.A. Ponnusami, A computationally efficient approach for generating RVEs of various inclusion/fibre shapes, *Compos. Struct.* 291 (2022), <https://doi.org/10.1016/j.compstruct.2022.115560>.
- [4] C. González, J.J. Vilatela, J.M. Molina-Aldareguía, C.S. Lopes, J. Llorca, Structural composites for multifunctional applications: Current challenges and future trends, *Prog. Mater Sci.* 89 (2017) 194–251, <https://doi.org/10.1016/j.pmatsci.2017.04.005>.
- [5] S. David Muzel, E.P. Bonhîn, N.M. Guimaraes, E.S. Guidi, Application of the finite element method in the analysis of composite materials: A review, *Polym.* 12 (4) (2020), <https://doi.org/10.3390/polym12040818>.
- [6] B. Hassani, E. Hinton, A review of homogenization and topology optimization i-homogenization theory for media with periodic structure, *Comput. Struct.* 69 (1998), <https://doi.org/10.1016/S0045-7949%2898%2900131-X>.
- [7] Y. Luo, Improved voigt and reuss formulas with the poisson effect, *Materials (basel)* 15 (16) (2022), <https://doi.org/10.3390/ma15165656>.
- [8] X. Zhang, S. Zhang, Y. Jia, C. Liu, X. Gao, F. Wang, Y. Song, A parameterized and automated modelling method for 3d orthogonal woven composite RVEs considering yarn geometry variations, *Compos. Struct.* 305 (2023), <https://doi.org/10.1016/j.compstruct.2022.116496>.
- [9] R. Bostanabad, Y. Zhang, X. Li, T. Kearney, L.C. Brinson, D.W. Apley, W.K. Liu, W. Chen, Computational microstructure characterization and reconstruction: Review of the state-of-the-art techniques, *Prog. Mater Sci.* 95 (2018) 1–41, <https://doi.org/10.1016/j.pmatsci.2018.01.005>.
- [10] C. Heinrich, M. Aldridge, A.S. Wineman, J. Kieffer, A.M. Waas, K. Shahwan, The influence of the representative volume element (RVE) size on the homogenized response of cured fiber composites, *Model. Simul. Mater. Eng.* 20 (7) (2012), <https://doi.org/10.1088/0965-0933/20/7/075007>.
- [11] V. Dubey, A. Noshadravan, A probabilistic upscaling of microstructural randomness in modeling mesoscale elastic properties of concrete, *Comput. Struct.* 237 (2020), <https://doi.org/10.1016/j.compstruc.2020.106272>.
- [12] L. Zhu, L. Sun, X. Wang, N. Li, Optimisation of three-dimensional hierarchical structures with tailored lattice metamaterial anisotropy, *Mater. Des.* 210 (2021), <https://doi.org/10.1016/j.matdes.2021.1110083>.
- [13] T. Dutta, S. Dey, S. Datta, D. Das, Designing dual-phase steels with improved performance using ANN and GA in tandem, *Comput. Mater. Sci.* 157 (2019) 6–16, <https://doi.org/10.1016/j.commatsci.2018.10.020>.
- [14] X. Ding, X. Hou, M. Xia, Y. Ismail, J. Ye, Predictions of macroscopic mechanical properties and microscopic cracks of unidirectional fibre-reinforced polymer composites using deep neural network (DNN), *Compos. Struct.* 302 (2022), <https://doi.org/10.1016/j.compstruct.2022.116248>.
- [15] M.V. Pathan, S.A. Ponnusami, J. Pathan, R. Pititongsawat, B. Erice, N. Petrinic, V. L. Tagarielli, Predictions of the mechanical properties of unidirectional fibre composites by supervised machine learning, *Sci. Rep.* 9 (1) (2019) 13964, <https://doi.org/10.1038/s41598-019-50144-w>.
- [16] M. Li, H. Zhang, S. Li, W. Zhu, Y. Ke, Machine learning and materials informatics approaches for predicting transverse mechanical properties of unidirectional CFRP composites with microvoids, *Mater. Des.* 224 (2022), <https://doi.org/10.1016/j.matdes.2022.111340>.
- [17] H.R. Attar, H. Zhou, A. Foster, N. Li, Rapid feasibility assessment of components to be formed through hot stamping: A deep learning approach, *J. Manuf. Process.* 68 (2021) 1650–1671, <https://doi.org/10.1016/j.jmapro.2021.06.011>.
- [18] H. Zhou, Q. Xu, Z. Nie, N. Li, A study on using image-based machine learning methods to develop surrogate models of stamp forming simulations, *J. Manuf. Sci. Eng.* 144 (2) (2022) 021012, <https://doi.org/10.1115/1.4051604>.
- [19] W. Yang, Y. Qiu, W. Liu, X. Qiu, Q. Bai, Defect prediction in laser powder bed fusion with the combination of simulated melt pool images and thermal images, *J. Manuf. Process.* 106 (2023) 214–222, <https://doi.org/10.1016/j.jmapro.2023.10.006>.
- [20] M. Li, S. Li, Y. Tian, Y. Fu, Y. Pei, W. Zhu, Y. Ke, A deep learning convolutional neural network and multi-layer perceptron hybrid fusion model for predicting the mechanical properties of carbon fiber, *Mater. Des.* 227 (2023), <https://doi.org/10.1016/j.matdes.2023.111760>.
- [21] C. Yang, Y. Kim, S. Ryu, G.X. Gu, Prediction of composite microstructure stress-strain curves using convolutional neural networks, *Mater. Des.* 189 (2020), <https://doi.org/10.1016/j.matdes.2020.108509>.
- [22] D.-W. Kim, J.H. Lim, S. Lee, Prediction and validation of the transverse mechanical behavior of unidirectional composites considering interfacial debonding through convolutional neural networks, *Compos. B Eng.* 225 (2021), <https://doi.org/10.1016/j.compositesb.2021.109314>.
- [23] Y. Xu, H. Weng, X. Ju, H. Ruan, J. Chen, C. Nan, J. Guo, L. Liang, A method for predicting mechanical properties of composite microstructure with reduced dataset based on transfer learning, *Compos. Struct.* 275 (2021), <https://doi.org/10.1016/j.compstruct.2021.114444>.
- [24] A. Olivier, M.D. Shields, L. Graham-Brady, Bayesian neural networks for uncertainty quantification in data-driven materials modeling, *Comput. Method Appl. Mech. Eng.* 386 (2021), <https://doi.org/10.1016/j.cma.2021.114079>.
- [25] V. Krokos, V.B. Xuan, S.P.A. Bordas, P. Young, P. Kerfriden, A bayesian multiscale CNN framework to predict local stress fields in structures with microscale features (preprint) (2022). <https://doi.org/10.48550/arXiv.2012.11330>.
- [26] V.A. Buryachenko, N.J. Pagano, R.Y. Kim, J.E. Spowart, Quantitative description and numerical simulation of random microstructures of composites and their effective elastic moduli, *Int. J. Solid Struct.* 40 (1) (2003) 47–72, [https://doi.org/10.1016/S0020-7683\(02\)00462-6](https://doi.org/10.1016/S0020-7683(02)00462-6).
- [27] L. Yang, Y. Yan, Z. Ran, Y. Liu, A new method for generating random fibre distributions for fibre reinforced composites, *Compos. Sci. Technol.* 76 (2013) 14–20, <https://doi.org/10.1016/j.compscitech.2012.12.001>.
- [28] S.-M. Park, J.H. Lim, M.R. Seong, D. Sohn, Efficient generator of random fiber distribution with diverse volume fractions by random fiber removal, *Compos. B Eng.* 167 (2019) 302–316, <https://doi.org/10.1016/j.compositesb.2018.12.042>.
- [29] T.J. Vaughan, C.T. McCarthy, A combined experimental-numerical approach for generating statistically equivalent fibre distributions for high strength laminated composite materials, *Compos. Sci. Technol.* 70 (2) (2010) 291–297, <https://doi.org/10.1016/j.compscitech.2009.10.020>.
- [30] D.J. O'Dwyer, N.P. O'Dowd, C.T. McCarthy, Numerical micromechanical investigation of interfacial strength parameters in a carbon fibre composite material, *J. Compos. Mater.* 48 (6) (2013) 749–760, <https://doi.org/10.1177/0021998313477172>.
- [31] P.J.E. Peebles, N-point correlation functions: Descriptive statistics, The large-scale structure of the universe1980. <https://doi.org/10.2307/j.ctvxpz4n.7>.
- [32] W. Zhou, A.C. Bovik, Mean squared error: Love it or leave it? A New Look at Signal Fidelity Measures, *IEEE Signal Processing Magazine* 26 (1) (2009) 98–117, <https://doi.org/10.1109/msp.2008.930649>.

- [33] H. Wang, H. Liu, Z. Ding, N. Li, Experimental and constitutive modelling studies of semicrystalline thermoplastics under solid-state stamp forming conditions, *Polym.* 228 (2021), <https://doi.org/10.1016/j.polymer.2021.123939>.
- [34] F. Chen, H. Ou, S. Gatea, H. Long, Hot tensile fracture characteristics and constitutive modelling of polyether-ether-ketone (PEEK), *Polym. Test.* 63 (2017) 168–179, <https://doi.org/10.1016/j.polymertesting.2017.07.032>.
- [35] E. Totry, C. González, J. Llorca, Prediction of the failure locus of C/PEEK composites under transverse compression and longitudinal shear through computational micromechanics, *Compos. Sci. Technol.* 68 (15–16) (2008) 3128–3136, <https://doi.org/10.1016/j.compscitech.2008.07.011>.
- [36] S.L. Omairey, P.D. Dunning, S. Sriramula, Development of an abaqus plugin tool for periodic RVE homogenisation, *Eng. Comput.* 35 (2) (2018) 567–577, <https://doi.org/10.1007/s00366-018-0616-4>.